

# Semi analytic approach to understanding the distribution of neutral hydrogen in the universe: Comparison of simulations with observations

T. Roy Choudhury  
tirth@iucaa.ernet.in

R. Srianand  
anand@iucaa.ernet.in

and

T. Padmanabhan  
paddy@iucaa.ernet.in

*IUCAA, Post Bag 4, Ganeshkhind, Pune 411 007, India.*

## ABSTRACT

Following Bi & Davidsen (1997), we perform one dimensional semi analytic simulations along the lines of sight to model the intergalactic medium (IGM). Since this procedure is computationally efficient in probing the parameter space – and reasonably accurate – we use it to recover the values of various parameters related to the IGM (for a fixed background cosmology) by comparing the model predictions with different observations. For the currently favoured LCDM model ( $\Omega_m = 0.4$ ,  $\Omega_\Lambda = 0.6$  and  $h = 0.65$ ), we obtain, using statistics obtained from the transmitted flux, constraints on (i) the combination  $f = (\Omega_B h^2)^2 / J_{-12}$ , where  $\Omega_B$  is the baryonic density parameter and  $J_{-12}$  is the total photoionisation rate in units of  $10^{-12} \text{s}^{-1}$ , (ii) temperature  $T_0$  corresponding to the mean density and (iii) the slope  $\gamma$  of the effective equation of state of the IGM at a mean redshift  $z \simeq 2.5$ . We find that  $0.8 < (T_0/10^4 \text{K}) < 2.5$  and  $1.3 < \gamma < 2.3$ . while the constraint obtained on  $f$  is  $0.020^2 < f < 0.032^2$ . A reliable lower bound on  $J_{-12}$  can be used to put a lower bound on  $\Omega_B h^2$ , which can be compared with similar constraints obtained from Big Bang Nucleosynthesis (BBN) and CMBR studies. We find that if  $J_{-12} > 1.2$ , the lower bound on  $\Omega_B h^2$  is in violation of the BBN value.

*Subject headings:* cosmology: large-scale structure of universe – intergalactic medium – quasars: absorption lines

## 1. Introduction

A significant fraction of the baryons at  $z \leq 5$  are found in the form of a diffuse intergalactic medium (IGM), which is usually probed through the absorption lines produced by them on the spectrum of the distant QSOs. It is believed that while the metal line systems (detected through Mg II or C IV doublets) seen in the QSO spectra could be associated with the halos of the intervening luminous galaxies (Bergeron & Boisse 1991; Steidel 1993), most of the low neutral hydrogen column density absorption lines (commonly called as ‘Ly $\alpha$ ’ clouds) are due to the low amplitude baryonic fluctuations in the IGM.

Probing the baryonic structure formation through Ly $\alpha$  absorption lines has two advantages. First, there are large number of absorption lines. Typically, one can observe more than a few hundreds of lines per unit redshift range along any one line of sight. This provides us with a large unbiased dataset, using which the statistical studies can be performed efficiently. The second advantage is that the Ly $\alpha$  absorption lines are more straightforward to model than, say, luminous galaxies. The modelling of galaxies is complicated by the fact that one has to take into account processes like the star formation, radiation feedback and so on; these processes are not that effective in the IGM, and one can ignore them at the first approximation.

The study of the IGM can – potentially – provide us with information about different aspects of the the baryonic structures the universe like (i) the mass power spectrum (Croft et al. 1998; Hui 1999; Croft et al. 1999), (ii) the total baryonic density ( $\Omega_B$ ) and the total photoionisation rate due to the local ionising background radiation ( $J$ ) and (iii) the reionisation history of the universe (Hui & Gnedin 1997).

There have been various numerical and semi analytical models in the literature for the IGM, all of which are based on the view that the Ly $\alpha$  clouds are small scale density fluctuations as predicted by the models of structure formation. The hydrodynamical simulations (Bond, Szalay & Silk 1988; Cen et al. 1994; Zhang, Anninos & Norman 1995; Hernquist et al. 1996; Miralda-Escudé et al. 1996; Riediger, Petitjean & Mücke 1998; Theuns, Leonard & Efstathiou 1998; Theuns et al. 1998; Davé et al. 1999) incorporate most of the ongoing physical processes in the IGM and hence they are necessary for understanding the evolution of the IGM. However, due to limited numerical resolution and computing power, they are able to probe only a small box size (10–20 Mpc). Hence people have tried to complement the numerical studies with analytic and semi analytic ones (Doroshkevich & Shandarin 1977; McGill 1990; Bi 1993; Bi, Ge & Fang 1995; Gnedin & Hui 1996; Hui, Gnedin & Zhang 1997; Bi & Davidsen 1997, hereafter BD; Choudhury, Padmanabhan & Srianand 2000, hereafter Paper I). The semi analytic models do not have problems related to limited numerical resolution or box sizes, and can be used to probe a wide range of parameters.

The numerical simulations suggest that *most* of the Ly $\alpha$  lines arise due to linear or quasi-linear density fluctuations. Therefore one can neglect the highly non-linear baryonic processes (like shock heating) as a first approximation. However, since a simple linear density evolution cannot produce the saturated Ly $\alpha$  systems, one cannot completely ignore the non-linear effects. The non-linear baryonic density can be calculated from the linear one using some approximation scheme, like the Zeldovich approximation (Doroshkevich & Shandarin 1977; McGill 1990; Hui, Gnedin & Zhang 1997), or the lognormal approximation (Bi 1993; Gnedin & Hui 1996; BD; Paper I). The neutral fraction is then estimated by considering the equilibrium between the rate of photoionisation due to background radiation and the rate of recombination estimated from the temperature defined through the equation of state. All these models depend on various IGM parameters such as  $\Omega_B$ ,  $J$ , equation of state and the Jeans length, as well as the cosmological parameters like  $\Omega_m, \Omega_\Lambda$ , etc.

Besides using these simplifying assumptions, BD realised that it is sufficient to simulate the IGM in 1D rather than in 3D. This increases the computing power drastically, and one can probe large box sizes (hundreds of Mpc) with high enough resolution. BD performed a detailed study of the evolution of the IGM from  $z = 2$  to 4. They also compared their predictions of column density distribution with hydrodynamical simulations and observations, and found a good agreement. In this work, we follow the idea proposed by BD and carry out semi analytic simulations of the low density IGM. The results obtained from such simulations are found to be in quite good agreement with various observations (as described in Section 5), thus indicating that the lognormal approximation might be a reasonable assumption for the low density IGM. We extend our studies to probe the parameter space and constrain the parameters for a particular redshift bin using different statistics obtained from the spectrum. Since the recovery of cosmological parameters is not possible with ill constrained IGM parameters (for a detailed discussion, see Paper I), we concentrate only on the parameters related to the IGM at a particular redshift (in this case,  $z = 2.41$ ). The parameters are the slope of the equation of state ( $\gamma$ ), the temperature corresponding to the mean baryonic density or the mean temperature ( $T_0$ ) [in this paper, we shall use the term ‘mean temperature’ to be equivalent to the temperature corresponding to the mean baryonic density] and a combination of the baryonic density parameter ( $\Omega_B$ ) and the total photoionisation rate due to the local ionising radiation field ( $J$ ), the combination being  $f = (\Omega_B h^2)^2 / J_{-12}$ , where  $J_{-12} = J / (10^{-12} \text{s}^{-1})$ . We find that different statistics are sensitive to different parameters, and hence they can be used simultaneously to constrain the parameter space.

In previous studies involving numerical simulations, the parameter  $f$  is usually determined by demanding that the simulated mean transmitted flux match with the observations (Rauch et al. 1997; McDonald et al. 2000a). Then for a given  $f$ , the constraints on  $\gamma$  and  $T_0$  are usually obtained by fitting the lower envelope of the  $N_{\text{HI}} - b$  scatter plot (Schaye

et al. 2000; Ricotti, Gnedin & Shull 2000; Bryan & Machacek 2000; McDonald et al. 2000b), where  $N_{\text{HI}}$  is the column density and  $b$  is the thermal velocity dispersion (defined as  $b = \sqrt{2k_{\text{B}}T/m_p}$ ). However, because of limited box size in the hydrodynamical simulations, the continuum of the transmitted flux is not well identified and this introduces errors in the calculation of the mean transmitted flux. In our approach, we constrain all the three parameters simultaneously using all the available transmitted flux statistics, thus utilising all the information available in the spectrum.

Section 2 gives the basic structure of the simulation strategy. Although the basic idea is the same as in BD, we repeat some of the details for completeness. This section also discusses about the various assumptions used at different stages. We discuss the various parameters used to model the simulation in Section 3. Section 4 contains a very brief discussion on the various statistical quantities studied in this paper. The next section contains the results, where we compare our simulations with available observational data and constrain  $f$ ,  $\gamma$  and  $T_0$ . Finally, we summarise our conclusions in section 6.

## 2. Basic Outline of the Simulation

We describe the structure of the numerical simulation in this section, which is essentially the same as in BD, for completeness and setting up the notation.

Let  $P_{\text{DM}}^{(3)}(k)$  denote the linear DM power spectrum in 3D at the present epoch ( $z = 0$ ). Then the power spectrum for any arbitrary  $z$  is given by

$$P_{\text{DM}}^{(3)}(k, z) = D^2(z)P_{\text{DM}}^{(3)}(k), \quad (1)$$

where  $D(z)$  gives the evolution of the linear density contrast. The linear baryonic power spectrum is related to the DM power spectrum through the relation (Fang et al. 1993)

$$P_B^{(3)}(k, z) = \frac{P_{\text{DM}}^{(3)}(k, z)}{(1 + x_b^2(z)k^2)^2}, \quad (2)$$

where

$$x_b(z) = \frac{1}{H_0} \left[ \frac{2\gamma k_{\text{B}}T_m(z)}{3\mu m_p \Omega_m (1+z)} \right]^{1/2} \quad (3)$$

is the Jeans length;  $\mu$  is the mean molecular weight of the IGM, given by  $\mu = 4/(8 - 5Y)$ , where  $Y$  is the helium weight fraction. (This relation assumes that the IGM consists mostly of fully ionised hydrogen and helium. In this paper, we take  $Y = 0.24$ .)  $T_m$  is the density averaged temperature of the IGM and  $\gamma$  is the ratio of specific heats.  $\Omega_m$  is the cosmological density parameter. Strictly speaking, equation (2) is valid only for the case where  $x_b$  is

independent of  $z$ , but it is shown by Bi, Borner & Chu (1992) that equation (2) is a good approximation for  $P_B^{(3)}(k, z)$  even when  $x_b$  has a redshift dependence.

At this point, it is appropriate to stress some features of the parameter  $T_m$ . The obvious interpretation of  $T_m$  will be as the mean temperature of the IGM,  $T_0$  (the temperature at the mean density), i.e.,  $T_m = T_0$ . However, according to BD, using  $T_0$  in equation (3) leads to a value of the linear baryonic density fluctuation,  $\sigma_B$ , larger than what we expect from hydrodynamical simulations. Hence, they suggested the use of a density averaged temperature. Since  $T_m$  appears only in the expression for the Jeans length (equation (3)), it can also be defined as the effective temperature which determines the Jeans length. It is clear that the combination  $\gamma T_m$  can, in principle, be fixed if  $\sigma_B$  is known through hydrodynamical simulations. In this work, we choose  $\sigma_B(z = 2.41)$  to be 1.34, which gives  $\gamma T_m = 5.115 \times 10^4 \text{K}$ . Our choice of  $\sigma_B(z = 2.41)$  is consistent with that of BD (see their Figure 3). Also, simulations of Carlberg & Couchman (1989) give  $\sigma_B(z = 2.8) = 0.953$ , but one should note that the power spectrum they used was normalised to a value that was 1.4 times smaller than ours. Furthermore, using a power spectrum normalised to a value 1.3 times larger than ours, Gnedin (1998) obtains  $\sigma_B(z = 2.85) = 2.25$ . All these values are consistent with our choice for which the value of Jeans length at  $z = 2.41$  is  $0.12 \Omega_m^{-1/2} h^{-1} \text{Mpc}$ . For the background cosmology with  $\Omega_m = 0.4, \Omega_\Lambda = 0.6$ , this corresponds to a velocity scale of  $22.3 \text{ km s}^{-1}$ . Since we shall be mainly concerned with a small redshift bin ( $\Delta z = 0.58$ ), the evolution of  $T_m$  should not affect the results significantly. Hence, we take  $T_m$  to be independent of  $z$ .

Once the power spectrum of linear density perturbations in 3D is obtained, one can obtain the corresponding power spectra for density (as well as velocity) perturbations in 1D. One can show that the baryonic power spectrum in 1D is given by

$$P_B^{(1)}(k, z) = \frac{1}{2\pi} \int_{|k|}^{\infty} dk' k' P_B^{(3)}(k', z). \quad (4)$$

while the power spectrum for linear velocity perturbations in 1D is

$$P_v^{(1)}(k, z) = \dot{a}^2(z) k^2 \frac{1}{2\pi} \int_{|k|}^{\infty} \frac{dk'}{k'^3} P_B^{(3)}(k', z), \quad (5)$$

where  $a$  is the scale factor and  $\dot{a}$  is given by the Friedman equations

$$\dot{a}^2(z) = H_0^2 \left[ \Omega_m(1+z) + \Omega_k + \frac{\Omega_\Lambda}{(1+z)^2} \right], \quad (6)$$

with

$$\Omega_k = 1 - \Omega_m - \Omega_\Lambda. \quad (7)$$

The density and the velocity fields are correlated with the correlation being given by

$$P_{\text{Bv}}^{(1)}(k, z) = i \dot{a}(z) k \frac{1}{2\pi} \int_{|k|}^{\infty} \frac{dk'}{k'} P_B^{(3)}(k', z). \quad (8)$$

To simulate the density and velocity fields in 1D for a particular redshift  $z$ , we follow the procedure given by Bi (1993). We start with two independent Gaussian fields,  $w_0(k)$  and  $u_0(k)$ , having unit power spectrum, i.e.,  $\langle w_0^*(k) w_0(p) \rangle = \langle u_0^*(k) u_0(p) \rangle = 2\pi \delta_{\text{Dirac}}(k - p)$ . We can then get two independent Gaussian fields having power spectra  $P_w(k, z)$  and  $P_u(k, z)$  respectively

$$w(k, z) = w_0(k) \sqrt{P_w(k, z)}, \quad u(k, z) = u_0(k) \sqrt{P_u(k, z)}. \quad (9)$$

We choose these power spectra to be of the following form (Bi 1993; BD)

$$P_w(k, z) = \beta^{-1}(k, z) \frac{1}{2\pi} \int_{|k|}^{\infty} \frac{dk'}{k'} P_B^{(3)}(k', z) \quad (10)$$

and

$$P_u(k, z) = \frac{1}{2\pi} \int_{|k|}^{\infty} dk' k' P_B^{(3)}(k', z) - P_w(k, z), \quad (11)$$

where

$$\beta(k, z) = \frac{\int_{|k|}^{\infty} (dk'/k'^3) P_B^{(3)}(k', z)}{\int_{|k|}^{\infty} (dk'/k') P_B^{(3)}(k', z)}. \quad (12)$$

The linear density and the velocity fields in the  $k$ -space are then given by

$$\delta_B(k, z) = w(k, z) + u(k, z), \quad (13)$$

$$v(k, z) = i \dot{a} k \beta(k, z) w(k, z). \quad (14)$$

The corresponding fields  $\delta_B(x, z)$  and  $v(x, z)$  in the real comoving space are obtained by using Fourier transforms. One should keep in mind that the above analysis is done in the framework of linear perturbation theory.

However, to study the properties of the IGM one has to take into account the nonlinearities in the density distribution and various physical processes such as shocks, radiation field, cooling etc. Detailed hydrodynamical modelling of IGM has shown that most of the low column density Ly $\alpha$  absorption (i.e.  $N_{\text{HI}} \leq 10^{14} \text{ cm}^{-2}$ ) are produced by regions that are either in the linear or in the weakly non-linear regime (Cen et al. 1994; Zhang et al. 1995; Hernquist et al. 1996; Miralda-Escudé et al. 1996; Theuns, Leonard & Efstathiou 1998; Theuns et al. 1998; Davé et al. 1999). The lower envelope of the column density,  $N_{\text{HI}} - b$  scatter plot (Schaye et al. 1999; Schaye et al. 2000) suggests that there is a well

defined relationship between the density and the temperature of the IGM (Hui & Gnedin 1997). Thus it is possible to model low column density systems using simple prescription for the non-linear density field and an equation of state.

Following BD, we take into account the effect of non-linearities of density perturbations by assuming the number density distribution of the baryons,  $n_B(x, z)$  to be a lognormal random field

$$n_B(x, z) = A e^{\delta_B(x, z)} \quad (15)$$

where  $\delta_B(x, z)$  is the linear density contrast in baryons, and  $A$  is a constant to be determined. The mean value of  $n_B(x, z)$  is given by

$$\langle n_B(x, z) \rangle \equiv n_0(z) = A \langle e^{\delta_B(x, z)} \rangle, \quad (16)$$

where  $n_0(z)$  is related to the baryonic density parameter  $\Omega_B$  through the relation

$$n_0(z) = \frac{\Omega_B \rho_c}{\mu_B m_p} (1+z)^3. \quad (17)$$

Here  $\rho_c = 1.8791 \times 10^{-29} h^2 \text{ cm}^{-3}$  is the critical density of the universe and  $\mu_B m_p$  is the mass per baryonic particle, given by  $\mu_B m_p = 4m_p/(4 - 3Y)$ . Hence, we get the value of the constant as

$$A = \frac{n_0(z)}{\langle e^{\delta_B(x, z)} \rangle} \quad (18)$$

and

$$n_B(x, z) = n_0(z) \frac{e^{\delta_B(x, z)}}{\langle e^{\delta_B(x, z)} \rangle}. \quad (19)$$

The lognormal distribution was introduced by Coles & Jones (1991) as a model for the non-linear matter distribution in the universe. Detailed arguments as to why this ansatz should be reasonable in studying non-linear density distribution can be found in Coles & Jones (1991), BD and Paper I. However, we would still like to stress some points regarding the use of the lognormal ansatz for baryons in the current context.

In the past, there have been attempts to use the lognormal distribution to model the dark matter. However, we now know (based on Non-linear Scaling Relations; see Nityananda & Padmanabhan 1994; Padmanabhan 1996) that any local mapping of the form  $\delta_{\text{NL}} = F[\delta_{\text{L}}]$  is bad for dark matter (also see Coles, Melott & Shandarin 1993). There is, however, a strong theoretical argument (see Paper I) which shows that lognormal produces the correct limits at the two extremes for *baryons*. At large spatial scales, where the density contrast is small ( $\delta_B \ll 1$ ), equation (19) reduces to  $n_B/n_0 \simeq 1 + \delta_B$ , which is just what we expect from linear theory. More importantly, on small scales, equation (19) becomes the isothermal hydrostatic solution, which describes highly clumped structures like intracluster gas,  $n_B \propto$

$\exp(-\mu m_p \psi_{\text{DM}}/\gamma k_B T)$ , where  $\psi_{\text{DM}}$  is the dark matter potential (Sarazin & Bahcall 1977). This gives an indication that even though the lognormal ansatz is poor for dark matter distribution, it might still work reasonably well for baryonic matter since it is correctly constrained at both extremes.

Comparison with full hydrodynamical simulations reinforces this conclusion. BD have used the results from the hydrodynamical simulations of Miralda-Escudé et al. (1996), and found that the baryonic density distribution can be well fitted by a lognormal function at  $z = 3$ . Also, the range of parameters for the IGM recovered by us and those by the full hydrodynamical simulations of McDonald et al. (2000a, b) agree quite well (as discussed later in Section 6). This shows that the lognormal assumption agrees with the hydrodynamical simulations as well.

The above arguments should convince the reader that the lognormal assumption, in spite of its limitations, provides us with a tool in studying the baryonic structure formation semi-analytically. No such approximation can reproduce the results obtained from the full hydrodynamical simulations exactly and their values lie in providing faster route to reasonably accurate results. Our attempts should be viewed in the backdrop of such a philosophy.

There is no obvious way to deal with the non-linearities in the velocity field, but fortunately this is not needed in the current work as can be seen from the following argument. The velocity field plays two separate roles in the context of our work. The first one is that the velocity determines the movement of the individual particles at a given instant of time, which in turn affects the underlying density field in the next time step. Mathematically this feature is represented by the Euler equation, which connects the density field to velocity field. Given any prescription for density field, the Euler equation implicitly leads to a consistent velocity field. Hence this dynamical effect of velocity field – viz. moving the mass to the right location – is indirectly taken into account in any prescription for non-linear density. In our case, the lognormal ansatz takes care of this feature. The second effect of the velocity field is purely kinematic – it shifts the positions of the absorption lines. In our work we will be using the thermal velocity dispersion  $b$  in the Voigt profile while analysing the lines. Since the Ly $\alpha$  absorption lines originate from quasi-linear density regions, the velocity field will be subdominant or of the same order as the thermal velocity dispersion  $b$ , which will be taken care of in our analysis.

Once the non-linear baryon density is obtained, it is trivial to get the fraction of hydrogen in the neutral form,  $f_{\text{HI}}$ , in the IGM by solving the ionisation equilibrium equation for hydrogen

$$\alpha(T)n_p n_e = \Gamma_{\text{ci}}(T)n_e n_{\text{HI}} + Jn_{\text{HI}}, \quad (20)$$

where  $\alpha(T)$  is the radiative recombination rate,  $\Gamma_{\text{ci}}(T)$  is the rate of collisional ionisation and



$J$  is rate of photoionisation for hydrogen (Black 1981);  $n_p, n_e$  and  $n_{\text{HI}}$  are the number densities of proton, electron and neutral hydrogen, respectively. In general, all these quantities are functions of  $z$  and all except  $J$  depend on the position  $x$  too. We shall parametrise  $J(z)$  by a dimensionless quantity  $J_{-12}(z)$ , defined by  $J(z) = J_{-12}(z)10^{-12}\text{s}^{-1}$ . For comparison, we mention that our  $J$  is equal to the quantity  $J_{21}G_1$  used by BD.

Black (1981) gives the approximate form of the recombination and ionisation rates as follows:

$$\frac{\alpha(T)}{\text{cm}^3\text{s}^{-1}} = \begin{cases} 4.36 \times 10^{-10}T^{-0.7573} & (\text{if } T \geq 5000\text{K}) \\ 2.17 \times 10^{-10}T^{-0.6756} & (\text{if } T < 5000\text{K}) \end{cases} \quad (21)$$

and

$$\Gamma_{\text{ci}}(T) = 5.85 \times 10^{-11}T^{1/2} \exp(-157809.1/T) \text{ cm}^3\text{s}^{-1}, \quad (22)$$

where  $T$  is in Kelvin. One can see that the expression for  $\alpha(T)$  diverges as  $T \rightarrow 0$  which needs to be regularised by a temperature cutoff at the lower end in numerical work. BD have used the photoionisation temperature as the minimum temperature, which is about  $10^4\text{K}$  (see also Theuns et al. 1998). In situations where  $T_0 > 10^4\text{K}$ , we too shall use the same value. However, when  $T_0 \leq 10^4\text{K}$ , we have taken the minimum temperature to be  $5000\text{K}$ .

The IGM contains mainly hydrogen, a smaller amount of helium (weight fraction,  $Y \sim 0.24$ ) and negligible amount of other heavier elements. In that case we can write  $n_e = \kappa n_p$ , where  $\kappa$  is a constant, greater than but very close to unity. However, in the following calculation we have neglected the presence of the heavier elements completely for simplicity. Let us define the neutral fraction of hydrogen,  $f_{\text{HI}}$  by

$$f_{\text{HI}} = \frac{n_{\text{HI}}}{n_B} = \frac{n_{\text{HI}}}{n_{\text{HI}} + n_p} \quad (23)$$

(we ignore the number density contributed by helium because, usually,  $n_{\text{He}}/n_B < 0.1$ ). Using equation (20) in (23), one gets

$$f_{\text{HI}}(x, z) = \frac{\alpha(T(x, z))}{\alpha(T(x, z)) + \Gamma_{\text{ci}}(T(x, z)) + J(z)/n_e(x, z)}. \quad (24)$$

We express  $n_e$  in terms of  $n_B$  by assuming that  $f_{\text{HI}} \ll 1$  and all the helium present is in the fully ionised form. In such case,

$$n_e/n_B \equiv \mu_e = 2(2 - Y)/(4 - 3Y). \quad (25)$$

Then,

$$n_{\text{HI}}(x, z) = \frac{\alpha(T(x, z))n_B(x, z)}{\alpha(T(x, z)) + \Gamma_{\text{ci}}(T(x, z)) + J(z)/(\mu_e n_B(x, z))} \quad (26)$$

We calculate  $T(x, z)$  using the polytropic equation of state

$$T(x, z) = T_0(z) \left( \frac{n_B(x, z)}{n_0(z)} \right)^{\gamma-1}, \quad (27)$$

where  $T_0(z)$  is the temperature of the IGM at the mean density. We now know the neutral hydrogen density at any redshift  $z$  along a particular axis. Our next goal is to find the density along a line of sight. This can be done by obtaining the density field along the backward light cone. In other words, we must obtain the quantity  $n_{\text{HI}}(x, z(x))$ , where  $x$  and  $z$  are related through the expression

$$x(z) = \int_0^z d_H(z') dz', \quad (28)$$

with

$$\begin{aligned} d_H(z) &= c \left( \frac{\dot{a}}{a} \right)^{-1} \\ &= \frac{c}{H_0} [\Omega_\Lambda + \Omega_m(1+z)^3 + \Omega_k(1+z)^2]^{-1/2}. \end{aligned} \quad (29)$$

Similarly one can also get the velocity field  $v(x, z(x))$  along the same LOS. Once the neutral hydrogen density and the velocity along the LOS is known, the Ly $\alpha$  absorption optical depth at redshift  $z_0$  can be obtained from the relation

$$\begin{aligned} \tau(z_0) &= \frac{cI_\alpha}{\sqrt{\pi}} \int dx \frac{n_{\text{HI}}(x, z(x))}{b(x, z(x))(1+z(x))} \\ &\times V \left[ \alpha, \frac{c(z(x) - z_0)}{b(x, z(x))(1+z_0)} + \frac{v(x, z(x))}{b(x, z(x))} \right], \end{aligned} \quad (30)$$

where

$$b(x, z(x)) = \sqrt{\frac{2k_B T(x, z(x))}{m_p}}, \quad (31)$$

$I_\alpha = 4.45 \times 10^{-18} \text{cm}^2$  and  $V$  is the Voigt function.  $I_\alpha$  is related to the Ly $\alpha$  absorption cross section through

$$\sigma_\alpha(\nu) = \frac{cI_\alpha}{b\sqrt{\pi}} V \left[ \alpha, \frac{c(\nu - \nu_\alpha)}{b\nu_\alpha} \right]. \quad (32)$$

For low column density regions, the natural broadening is not that important, and the Voigt function reduces to a simple Gaussian

$$V\left[\alpha, \frac{\Delta v}{b}\right] \simeq \exp\left(-\frac{(\Delta v)^2}{b^2}\right). \quad (33)$$

Since we are mostly dealing with weakly non-linear regimes, where the densities are not too high, this approximation does not introduce any significant error in the final results. The optical depths obtained above are used to get the final line of sight spectrum.

### 3. Model Parameters

Following Paper I, the model parameters can be broadly divided into two classes, namely, those related to the background cosmology and those related to the baryonic IGM. In Paper I, we have considered various CDM cosmological models (SCDM, LCDM, OCDM) and a range of IGM parameters, and have found that the parameters related to the background cosmology cannot be constrained uniquely with ill defined IGM parameters. Consequently, the approach taken in this paper is to use the available observations for constraining the IGM related parameters under the framework of most favoured structure formation scenario. We consider the following parameters for the LCDM model. The CDM power spectrum in 3D is taken to be (Efstathiou, Bond & White 1992)

$$P_{\text{DM}}^{(3)}(k) = \frac{A_{\text{DM}}k}{(1 + [a_1k + (a_2k)^{1.5} + (a_3k)^2]^\nu)^{2/\nu}} \quad (34)$$

where  $\nu = 1.13$ ,  $a_1 = (6.4/\Gamma)h^{-1}$  Mpc,  $a_2 = (3.0/\Gamma)h^{-1}$  Mpc,  $a_3 = (1.7/\Gamma)h^{-1}$  Mpc and  $\Gamma = \Omega_m h$ . The normalisation parameter  $A_{\text{DM}}$  is fixed through the value of  $\sigma_8$  (the rms density fluctuation in spheres of radius  $8 h^{-1}$  Mpc) which is taken to be  $\sigma_8 = 0.79$ . The other model parameters are:

$$\Omega_m = 0.4, \Omega_\Lambda = 0.6, h = 0.65. \quad (35)$$

The values of  $\Omega_m$  and  $\Omega_\Lambda$  are consistent with the best fitted parameters of Ostriker & Steinhardt (1995). The value of  $\sigma_8$  is obtained from the first year COBE normalisation (Kofman, Gnedin & Bahcall 1993). This value is also consistent with those obtained from the observed local abundance of clusters by Eke, Cole & Frenk (1996). An identical LCDM model is considered in the hydrodynamical simulations by Miralda-Escudé et al. (1996).

Once the cosmology is fixed, we turn our attention towards the parameters related to the baryons.

1. Slope of the effective equation of state ( $\gamma$ ): It is known that the value of  $\gamma$ , at any given epoch, depends on the reionisation history of the universe (Theuns et al. 1998, Hui & Gnedin 1997). The value of  $\gamma$  and its evolution are still quite uncertain. Using Voigt profile fits to the observed Ly $\alpha$  absorption lines one can in principle obtain the value of  $\gamma$ . In this work, we will keep  $\gamma$  as a free parameter and ignore its redshift evolution.
2. Mean temperature ( $T_0(z)$ ): Mean temperature of the IGM is decided by the various heating and cooling processes. In addition to the reionisation history local radiation field will also affect the value of  $T_0(z)$ . In the case of full hydrodynamical models,

the mean temperature is estimated self-consistently by considering various processes. However in our approach we consider the mean temperature as a free parameter. We also take it as independent of  $z$  within the small redshift bin we consider.

3.  $\Omega_B h^2$  and  $J_{-12}(z)$ : If one compares the typical values of the three quantities in the denominator in the right hand side of equation (26), one can verify that  $\alpha(T)$  and  $\Gamma_{\text{ci}}(T)$  are much smaller compared to  $J/n_B$  (typically, for  $T \sim 5 \times 10^4 \text{K}$ ,  $\alpha \sim 10^{-13} \text{cm}^3 \text{s}^{-1}$ ,  $\Gamma_{\text{ci}} \sim 10^{-14} \text{cm}^3 \text{s}^{-1}$  and  $J(z)/n_B \sim 10^{-5} \text{cm}^3 \text{s}^{-1}$ ). This means that we can write  $n_{\text{HI}} \simeq \alpha n_B^2 / J$ . Since  $n_B \propto n_0 \propto \Omega_B h^2$  and  $J(z) \propto J_{-12}(z)$ , we see that only the combination  $f(z) = (\Omega_B h^2)^2 / J_{-12}(z)$  appears in the expression for optical depth. We shall treat this quantity  $f(z)$  as a free parameter. We shall also assume that the photoionisation rate does not depend on  $z$  (at the least, it does not vary considerably within the small redshift bin we are interested in). This will make  $f$  independent of  $z$ .

So, we finally end up with three free parameters, namely  $\gamma$ ,  $T_0$ , and  $f$ .

#### 4. Statistical Quantities: Definitions

We perform various statistics on our simulated spectrum, as one usually does with the real data, to constrain various parameters of our model.

From the spectrum, one can immediately calculate the mean transmitted flux ( $\bar{F}$ ) and the rms flux fluctuations ( $\sigma_F^2$ ). The transmitted flux data can also be used to obtain three important statistics (McDonald et al. 2000a). These are: (i) the probability distribution function (PDF) for the transmitted flux, (ii) the correlation function of the transmitted flux, defined as  $\xi(\Delta v) = \langle (F(v) - \bar{F})(F(v + \Delta v) - \bar{F}) \rangle$  and (iii) the flux power spectrum ( $P_F(k)$ ). The power spectrum is calculated using the Lomb periodogram technique (Lomb 1976; Scargle 1982; Press et al. 1992) and the normalisation used is the same as mentioned in McDonald et al. (2000a), i.e.,  $\sigma_F^2 = \int_{-\infty}^{\infty} (dk/2\pi) P_F(k)$ . The advantage in the case of statistics obtained from transmitted flux is that the numerical procedure is quite fast. We use these statistics for constraining the parameter space.

For a set of most favourable values of parameters, we decompose the spectrum into individual lines using Voigt profile analysis, and use them to check our predictions with the observations. The statistics used for this purpose are (i) the number of lines (absorbers) per unit redshift range ( $dN/dz$ ) and the column density distribution ( $f(N_{\text{HI}})$ ), defined as the number of lines (absorbers) per unit redshift path per unit column density range (Kim et al. 1997), (ii) the distribution of the  $b$  parameter and (iii) the two point correlation function for the absorbers, defined as  $\xi_{\text{cloud}}(\Delta v) = [N_{\text{sim}}(\Delta v) / N_{\text{exp}}(\Delta v)] - 1$ , where  $N_{\text{sim}}(\Delta v)$  is the

number of cloud pairs with a velocity separation  $\Delta v$  obtained from the simulated data and  $N_{\text{obs}}(\Delta v)$  is the number of pairs expected from a random distribution of clouds (Sargent et al. 1980; Webb 1987; Srianand & Khare 1994; Kulkarni et al. 1996; Srianand 1996; Khare et al. 1997; Kim et al. 1997; Cristiani et al. 1997).

## 5. Results

In this paper, we have concentrated our studies in the redshift range 2.09–2.67. This range corresponds to a box size of  $436 h^{-1}$  Mpc (for the cosmology we are considering), which is virtually impossible to probe in a full 3D hydrodynamical simulation with high enough resolution. The number of grid points used in this work along the line of sight was  $2^{15}$ , which were equispaced in the comoving coordinate  $x$ . The simulated flux data was then resampled with  $\Delta\lambda=0.04 \text{ \AA}$  and a random noise of (S/N)=30 was added, exactly as is done with the observed data. We mention here that even if we increase the number of points (i.e., try to achieve a better resolution), the resampling mentioned above would make sure that the statistics obtained from the transmitted flux are not affected. We found that the continuum of the spectrum is quite well defined at this redshift, and hence it was not necessary to make any extra normalisation.

### 5.1. Comparison with observations

We use various statistics obtained from the observational data given by McDonald et al (2000a). In the redshift range 2.09–2.67, they have considered data from 5 QSOs, namely, Q2343+123 ( $z_{\text{em}} = 2.52$ ), Q1442+293 ( $z_{\text{em}} = 2.67$ ), KP77: 1623+2653 ( $z_{\text{em}} = 2.526$ ), Q1107+485 ( $z_{\text{em}} = 3.00$ ) and Q1425+604 ( $z_{\text{em}} = 3.20$ ). Each of these quasar sight lines span different regions of the redshift interval, and hence all the redshifts are not equally weighted in the above mentioned redshift range. However in our simulated data we cover the same redshift range giving equal weightage. We have confirmed that the correction introduced due to this uneven weightage in observed data is negligible (i.e., much below typical observational errors).

The allowed range for various parameters are obtained by demanding that the simulated data pass through most of the observed points, within the allowed  $1\sigma$  error limits. The value of  $f$  is strongly constrained between  $0.020^2$ – $0.032^2$  (regardless of the value of  $\gamma$  and  $T_0$ ). In the above range of  $f$ , we consider models with  $f = 0.023^2, 0.026^2, 0.029^2$  and obtain constraints on  $T_0$  and  $\gamma$  so that all the observed statistics obtained from the transmitted flux

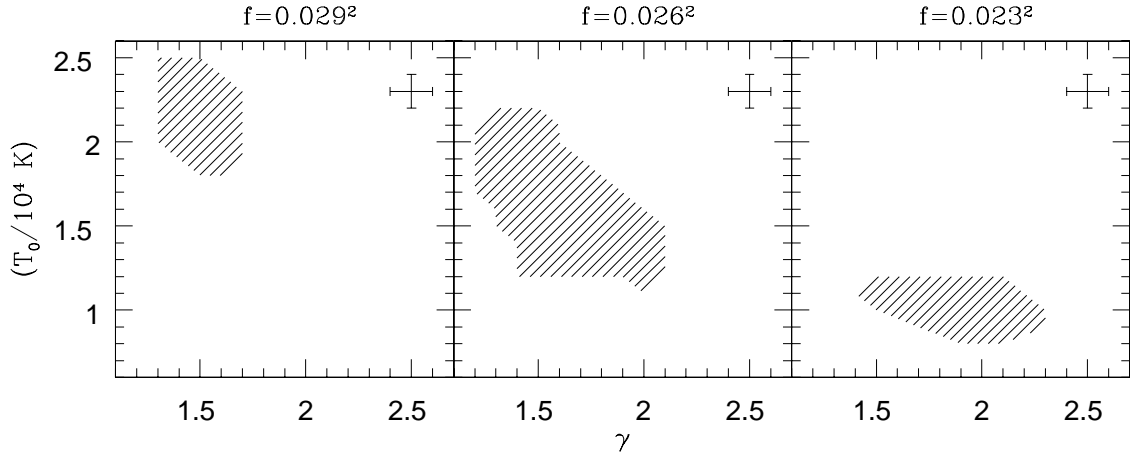


Fig. 1.— The constraints obtained in the  $\gamma - T_0$  space for different values of  $f$ , using transmitted flux statistics. The shaded regions denote the range allowed by observations. The boundaries are uncertain by an amount 0.1 along  $\gamma$  axis and by 1000K along the  $T_0$  axis because of finite sampling, which is shown by a cross at the upper right hand corners of the panels.

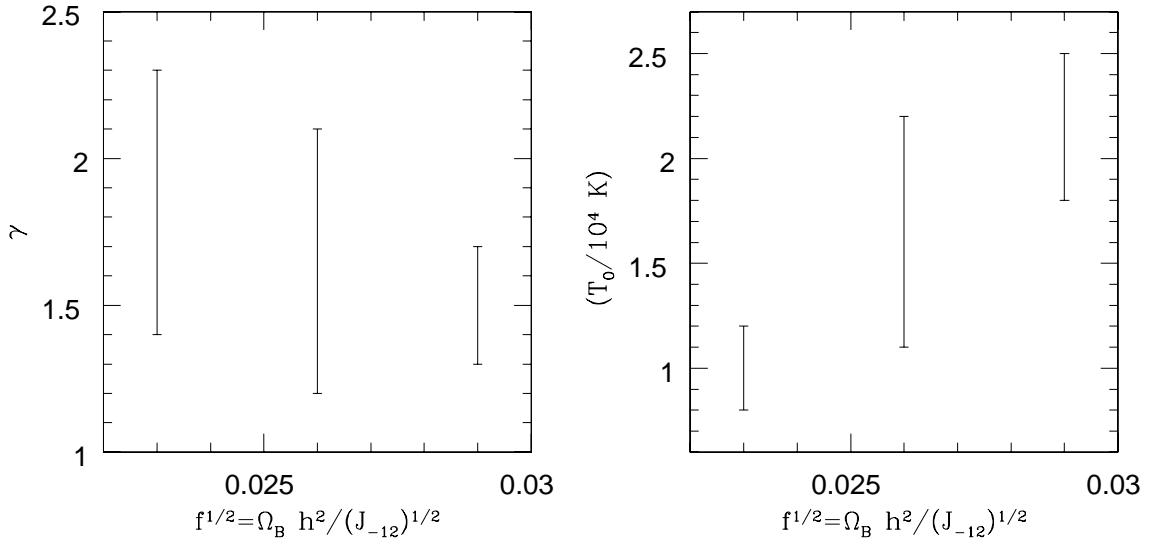


Fig. 2.— The left panel shows the allowed range of  $\gamma$  for different values of  $f$ , regardless of the value of  $T_0$ . The right panel shows the allowed range of  $T_0$ , regardless of  $\gamma$ . The ranges are obtained using transmitted flux statistics only.

are consistently reproduced.

The constrained parameter space for these three values of  $f$  is shown in Figure 1. (We mention here that due to finite sampling of the parameter space, the boundaries of the allowed region are uncertain by an amount 0.1 along the  $\gamma$  axis and by 1000K along the  $T_0$  axis; this error budget is indicated by a cross at the right top corner of the panels.) It is obvious that as we go to lower values of  $f$ , the observations allow lower values of  $T_0$  and higher values of  $\gamma$ . For example,  $1.4 < \gamma < 2.3$ ,  $0.8 \times 10^4\text{K} < T_0 < 1.2 \times 10^4\text{K}$  for  $f = 0.023^2$  whereas  $1.3 < \gamma < 1.7$ ,  $1.8 \times 10^4\text{K} < T_0 < 2.5 \times 10^4\text{K}$  for  $f = 0.029^2$ . It is also seen that the area of the allowed region is maximum for  $f = 0.026^2$  and is smaller for higher or lower values of  $f$ . We mention here that the allowed region is practically zero for  $f < 0.020^2$  and  $f > 0.032^2$ .

The limits on  $\gamma$  and  $T_0$  for  $f$  in the range  $0.023^2$ – $0.029^2$  are shown in Figure 2. The left panel shows the allowed range of  $\gamma$  regardless of the value of  $T_0$ , the right panel shows that for  $T_0$ , regardless of  $\gamma$ .

Although the observations allow  $f$  in the range  $0.020^2$  to  $0.032^2$ , we find that the match between simulations and observations is best for  $f \sim 0.026^2$ . We calculated the  $\chi^2$  of the three statistics for different parameter values and found that they are comparatively lower for  $f = 0.026^2$  than for higher or lower values of  $f$ . Hence, in what follows, we shall concentrate on  $f = 0.026^2$ , and see explicitly how all the statistics compare with observations. In Figure 3, we show the comparison between simulations and observations for various transmitted flux statistics for some particular values of  $\gamma$  and  $T_0$ . The point to be noted here is that *our simulations are able to match the observations for all the three statistics for a particular range of parameter values*. The results obtained using hydrodynamical simulations fail to match the observations for the flux correlation function and the power spectrum simultaneously (McDonald et al. 2000a), mainly because of the lack of power at large scales (due to limited box size). As discussed earlier, our semi analytic simulations probe large box sizes without compromising on the resolution, and hence we are able to match both the statistics simultaneously. We mention here that the typical length scales probed by both the correlation function and the power spectrum is about  $100 h^{-1}$  Kpc to  $25 h^{-1}$  Mpc.

The left panel shows the limit on  $T_0$  for  $\gamma = 1.5$ . It is clear that for  $T_0 \geq 2.2 \times 10^4\text{K}$ , the value of  $\bar{F}$  is larger than what is allowed by the observations. At temperatures higher than this, the recombination rate is so low that the neutral fraction of hydrogen reduces and hence the transmitted flux goes above the allowed limit. Furthermore, we can see that the power spectrum also restricts the allowed range of  $T_0$  between  $(1.2\text{--}2.2) \times 10^4\text{K}$ . At higher (lower) temperatures, the power at smaller scales are reduced (enhanced) due to excess (less) Voigt

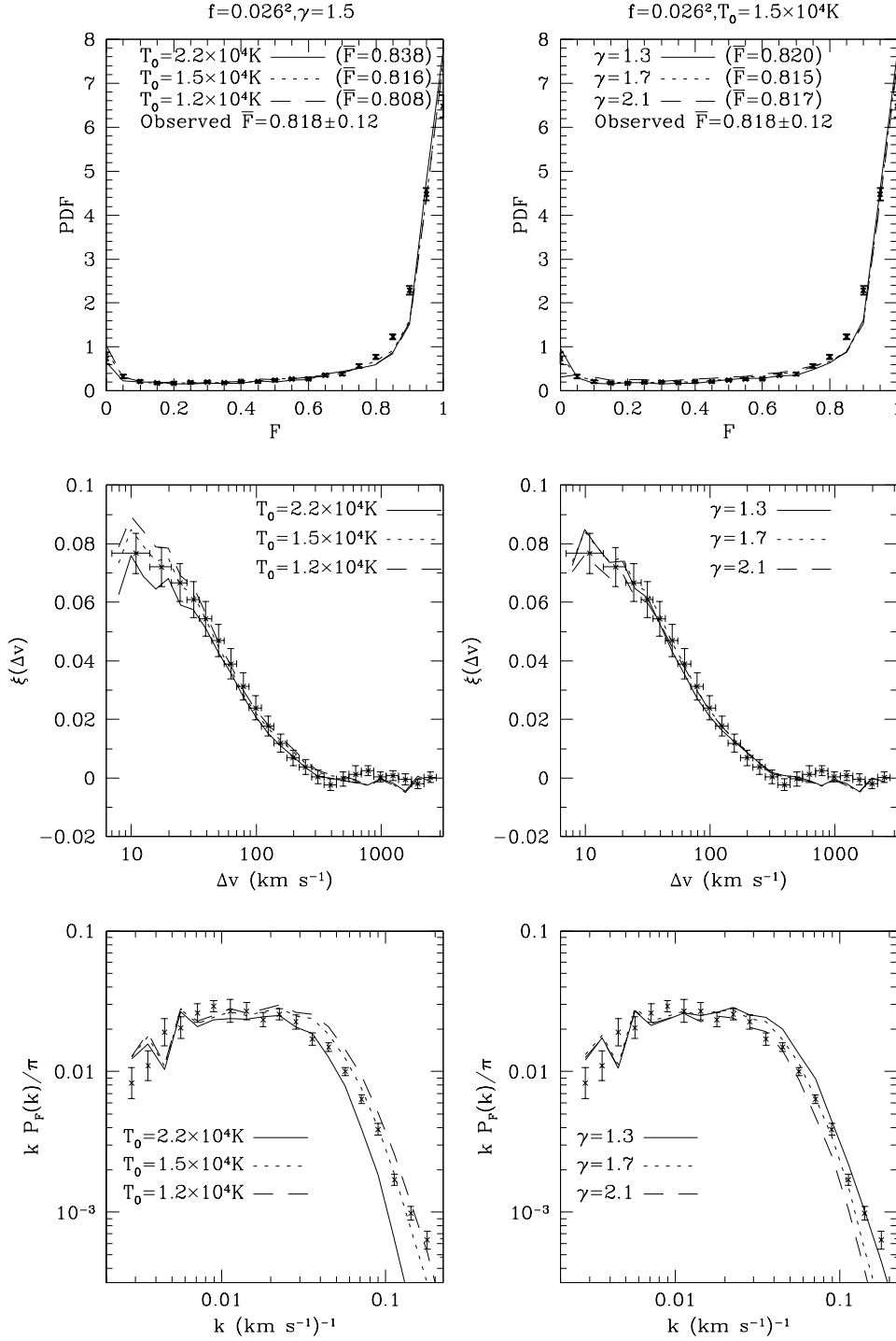


Fig. 3.— The comparison between simulations and observed results for  $f = 0.026^2$ . The points with errorbars are the observed data points (McDonald et al. 2000a). In the left panel, we show the limits on  $T_0$  for a particular  $\gamma$  (in this case, 1.5), and the right panel shows the limit on  $\gamma$  for  $T_0 = 1.5 \times 10^4 \text{K}$ .



profile smoothing. From the way it is defined (see the previous section), the normalisation of the correlation function depends on  $T_0$ . The correlation curves go up when  $T_0$  is decreased. However, since the errorbars on  $\xi$  are comparatively larger, the correlation curve does not impose any further constraints.

The right panel shows the limit on  $\gamma$  for  $T_0 = 1.5 \times 10^4 \text{K}$ . (We mention here again that while changing the value of  $\gamma$ , we change the value of  $T_m$  also, such that the combination  $\gamma T_m$ , and hence the Jeans length remains unchanged.) The effect of increasing  $\gamma$  is to increase the range of temperature in the IGM for a given baryon density range (Paper I). This actually reduces the range in the recombination rate and hence the range of neutral hydrogen density. Since a large  $\gamma$  means less fluctuations in the neutral hydrogen densities, there are less number points having extreme values of the flux, as one can see from the PDF. It is clear that one can rule out  $\gamma > 2.1$  from the PDF. Also, one can see from the flux power spectrum curve that there is a reduction (enhancement) in the small scale power for larger (smaller) values of  $\gamma$ . This restricts  $\gamma$  between 1.3–2.1. The correlation curve is quite insensitive to  $\gamma$  as compared to the other two parameters, and hence it does not impose any further constraints. Since the normalisation of the correlation function depends on  $f$  and  $T_0$  but not on  $\gamma$ , the correlation curves are comparatively less sensitive to  $\gamma$ .

In the allowed ranges of parameters, the match between observations and our simulations is quite good for all the three statistics obtained from the transmitted flux. We did not compare the simulated flux power spectrum with observations for smaller scales ( $k > 0.2 \text{ km s}^{-1}$ ). The reason for this is the presence of narrow metal lines in the observed spectra, which contribute to the small scale power. Detailed discussion regarding this aspect can be found in McDonald et al. (2000a).

Once we have constrained the range of  $\gamma - T_0$  space for  $f = 0.026^2$ , it is worth checking whether we can match the observed statistics obtained from the Voigt profile decomposition of the spectrum. We have used the standard Voigt profile routine (Khare et al. 1997) to decompose the observed spectrum into clouds. The minimum number of components required to fit an absorption line is constrained by the  $\chi^2$  minimisation. For this purpose, we concentrate on a particular value of  $T_0 = 1.5 \times 10^4 \text{K}$  and  $\gamma = 1.7$ . For obtaining the statistics, we take lines centered around  $z = 2.26$ , so as to mimic the observed data of Kim et al. (1997) at  $z = 2.31$ . The redshift interval considered is  $\Delta z = 0.26$ . Figure 4 shows the comparison between observations and simulations for the  $b$  distribution. The mean  $b$  of the simulated distribution is  $35.19 \text{ km s}^{-1}$ , whereas that of the observed distribution is  $36.35 \text{ km s}^{-1}$ . We have performed a  $\chi^2$  statistics for the two distributions, and found  $\chi^2/\nu = 0.61$  (with  $\nu = 34$ , 96.3 per cent likelihood).

We perform the same exercise with the column density distribution  $f(N_{HI})$ . The com-

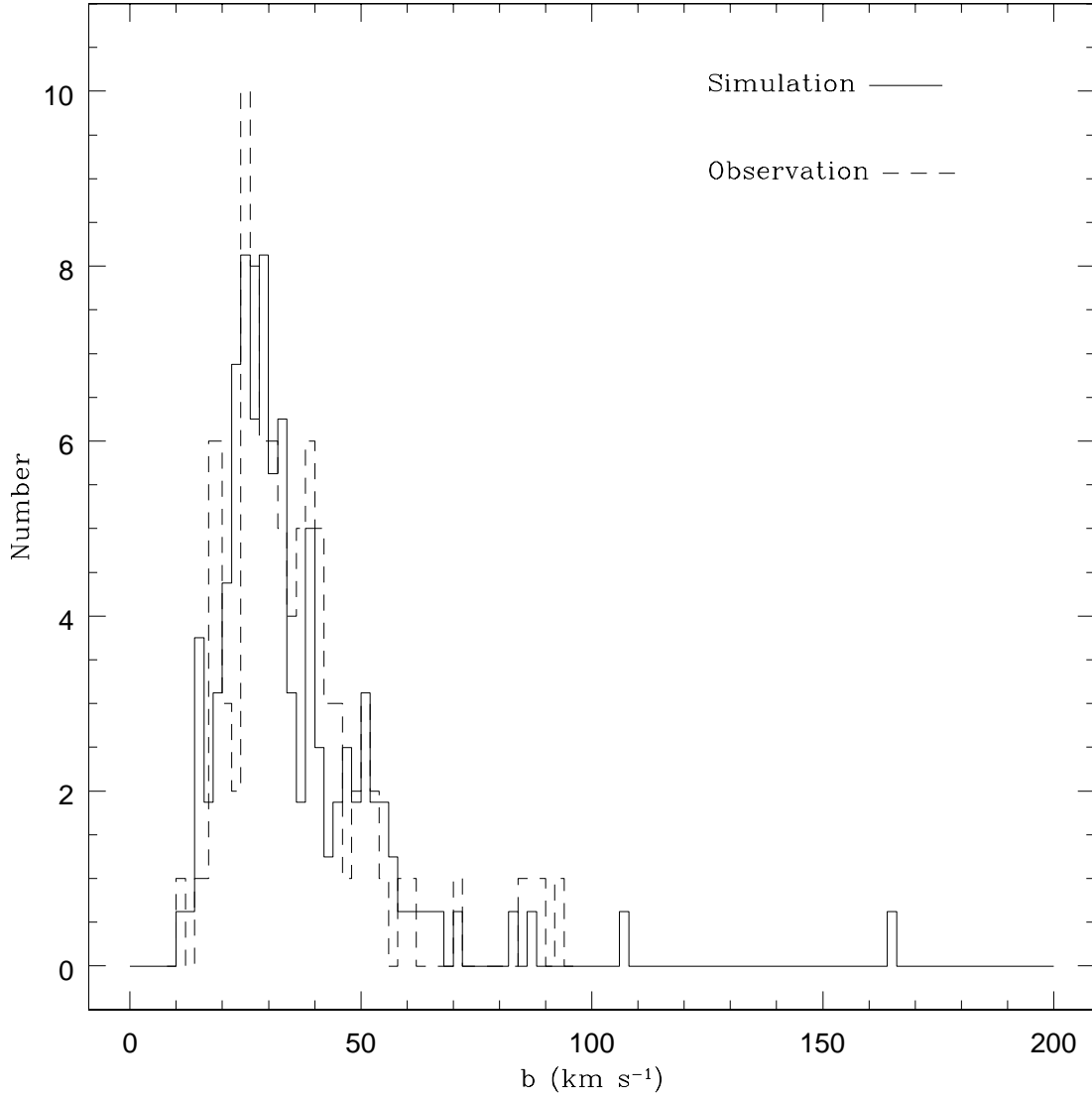


Fig. 4.— Comparison of the observed  $b$  distribution with the simulations. Here,  $\gamma = 1.7$ ,  $T_m = 3.01 \times 10^4 \text{K}$ ,  $f = 0.026^2$  and  $T_0 = 1.5 \times 10^4 \text{K}$ . The observed data is for  $z = 2.31$ , taken from Kim et al. (1997).

parison between simulations and observations is shown in Figure 5. Usually, one assumes a power law distribution for  $f(N_{HI})$ , i.e.,  $f(N_{HI}) \propto N_{HI}^{-\beta_{HI}}$ . In our case, we obtain the slope by carrying out a maximum likelihood analysis (Srianand & Khare 1996) where effects of binning are avoided. We present the distribution in the figure in the binned form for the purpose of better visualisation. The slope of the column density distribution,  $\beta_{HI}$ , in the column density range  $12.8 \leq \log(N_{HI}/\text{cm}^{-2}) \leq 16.0$  obtained from simulations is  $1.31 \pm 0.13$ ; the corresponding quantity obtained from observations is around 1.35 (Kim et al. 1997). One can also compare the values of  $dN/dz$  obtained from simulations and observations. For  $13.77 \leq \log(N_{HI}/\text{cm}^{-2}) \leq 16.0$ , we get  $dN/dz = 141.06 \pm 23.19$ . The corresponding number obtained from observations is between 63.09 and 100.00 (see Figure 2 of Kim et al. 1997). For  $13.1 \leq \log(N_{HI}/\text{cm}^{-2}) \leq 14.0$ , we obtain  $dN/dz = 202.06 \pm 27.75$ , which is well within the observed limits of 158.49 and 223.87.

The correlation function for the clouds  $\xi_{\text{cloud}}(\Delta v)$  obtained from our simulations is shown in Figure 6, for two different column density thresholds. We have used a velocity bin of 50  $\text{km s}^{-1}$ . We have also marked the  $1\sigma$  and  $2\sigma$  significance levels in the figure, obtained using a Poisson distribution. We can see that there is virtually no correlation above  $2\sigma$  significance level when the column density threshold is low ( $N_{HI} > 12.8 \text{ cm}^{-2}$ ). There is a clear positive correlation ( $2.78\sigma$  significance) in the velocity bin around  $\Delta v = 125 \text{ km s}^{-1}$  for clouds with  $N_{HI} > 10^{13.8} \text{ cm}^{-2}$ . The dependence of clustering on the strength of the lines was noted by Cristiani et al. (1997) and Srianand (1997). Kim et al. (1997) find a positive correlation of  $2.8\sigma$  significance at the velocity bin 50–100  $\text{km s}^{-1}$  in the observed data. Cristiani et al. (1997) too find a positive correlation of about  $7\sigma$  significance at  $\Delta v = 100 \text{ km s}^{-1}$ , in a wide redshift range  $1.7 < z < 3.1$  using a much larger number of samples.

While concentrating on the parameter values  $f = 0.026^2$  and  $T_0 = 1.5 \times 10^4 \text{K}$ , we would like to see the effect of  $\gamma$  on the statistics obtained from the Voigt profile decomposition. The comparison of the  $b$ -distribution for different values of  $\gamma$  is given in Table 1. We have performed a  $\chi^2$  test, the results being shown in the same table. The mean  $b$  increases with  $\gamma$ , which is due to the fact that the range of temperatures is higher for large  $\gamma$ .

Table 1: Comparison between simulated  $b$  distribution and observations for  $f = 0.026^2$ ,  $T_0 = 1.5 \times 10^4 \text{K}$  and different values of  $\gamma$ . The observed mean value of  $b$  is  $36.35 \text{ km s}^{-1}$  at  $z = 2.31$ .

$\gamma$	$\chi^2/\nu$ (likelihood)	Mean $b$ ( $\text{km s}^{-1}$ )
1.5	0.70 (90.2%)	34.90
1.7	0.61 (96.3%)	35.19
2.1	0.92 (59.5%)	37.39

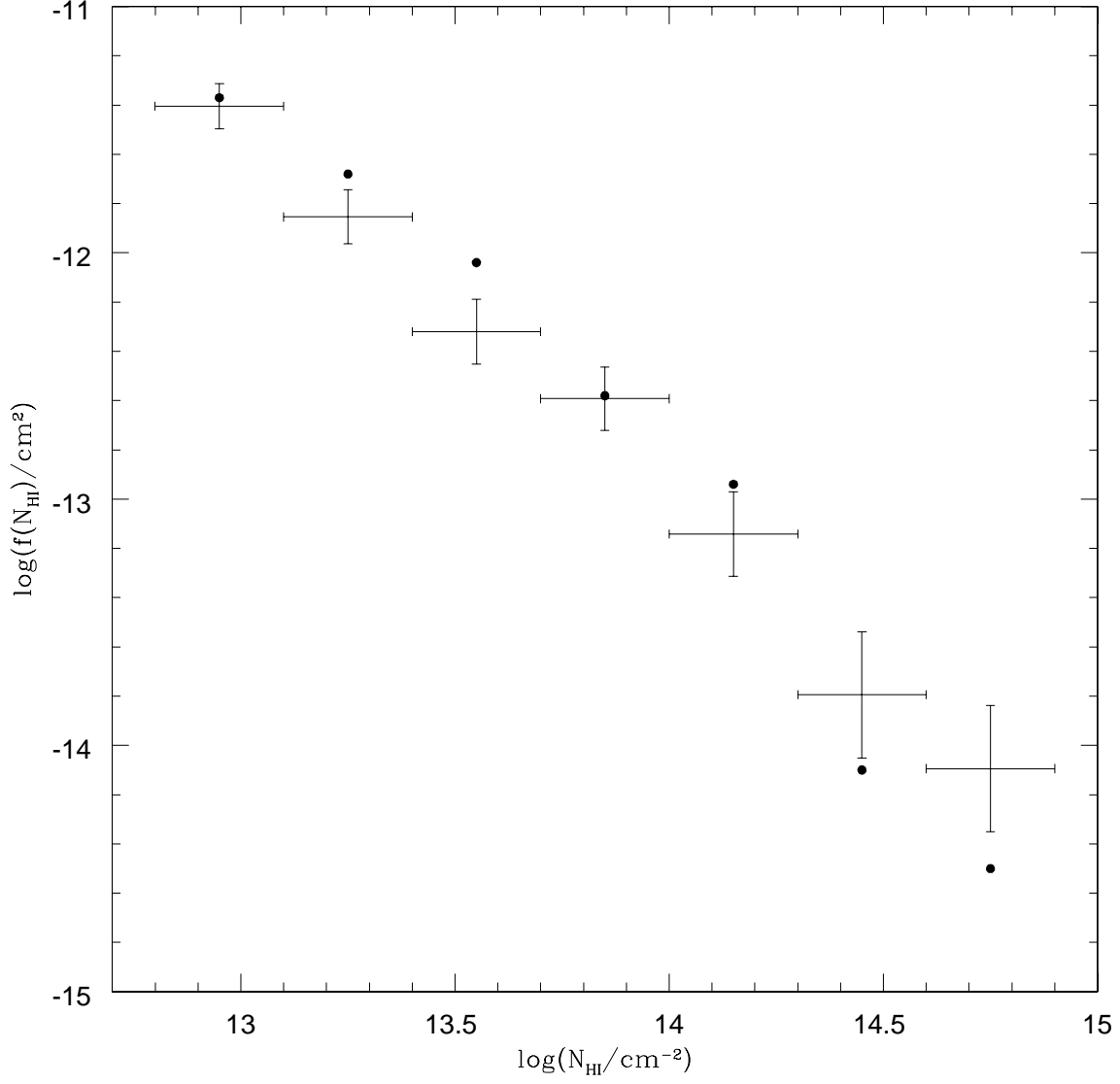


Fig. 5.— Comparison of the observed column density distribution with the simulations. The points in the figure are the observed data. The error bars indicate the values obtained from simulations. Here,  $\gamma = 1.7$ ,  $T_m = 3.01 \times 10^4\text{K}$ ,  $f = 0.026^2$  and  $T_0 = 1.5 \times 10^4\text{K}$ .

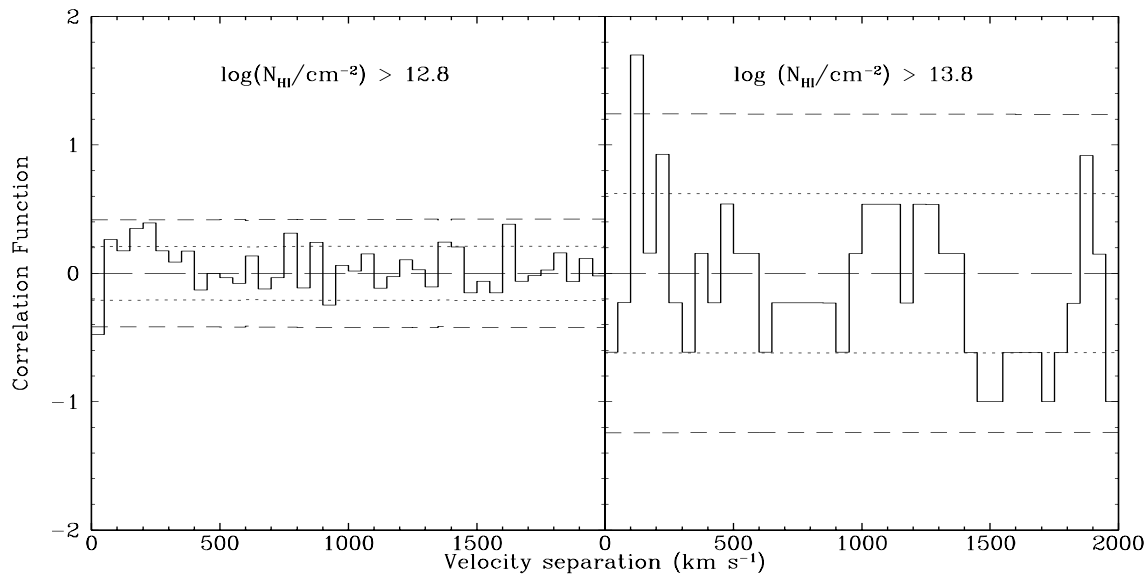


Fig. 6.— The correlation function for clouds obtained from simulations with  $\gamma = 1.7$ ,  $T_m = 3.01 \times 10^4\text{K}$ ,  $f = 0.026^2$  and  $T_0 = 1.5 \times 10^4\text{K}$ . The results are presented for two different column density thresholds. The dotted and the short-dashed lines show the  $1\sigma$  and  $2\sigma$  deviation from random distribution, respectively. The velocity bin width used is  $50 \text{ km s}^{-1}$ .

Next, we compare the simulated column density distribution,  $f(N_{\text{HI}})$  with observations for different values of  $\gamma$ . Table 2 gives the values of the slope of the distribution,  $\beta_{\text{HI}}$  in the column density range  $12.8 \leq \log(N_{\text{HI}}/\text{cm}^{-2}) \leq 16.0$  for different  $\gamma$ . The distribution becomes steeper as we increase  $\gamma$ . This is consistent with semi analytic results of Paper I. It is very clear that the slope for  $\gamma < 1.5$  ( $\gamma > 2.1$ ) is too flat (steep) to match the observations, even within error limits. This is somewhat consistent with what we find from the  $b$ -distribution above. We have checked and found that the  $dN/dz$  for  $13.77 \leq \log(N_{\text{HI}}/\text{cm}^{-2}) \leq 16.0$  for different values of  $\gamma$  is well within the observed range.

Finally, we discuss the correlation functions. Table 3 shows the correlation function within  $100 \text{ km s}^{-1} < \Delta v < 150 \text{ km s}^{-1}$  for different values of  $\gamma$ . There is a slight increase in the correlation amplitude as one increases  $\gamma$ . One can, in principle, use this trend to constrain the value of  $\gamma$  through correlation function. However, here we cannot do so because of the large errors ( $\sigma \sim 0.6$ ). We have taken the same number of lines as is done in the observations (about 100–140). Consequently, the errors are large and the correlation functions are consistent with observations for a wide range of parameter values.

To summarise, we have shown that, for some particular parameter range, our model is consistent with all of the observations (within error limits) obtained from the transmitted flux and from the Voigt profile decomposition of the observed spectrum. This justifies our approach of modelling the IGM using the lognormal approximation. We have also shown that it is possible to put stringent limits on the  $\gamma - T_0$  plane for a given  $f$  using transmitted flux statistics only.

## 6. Discussions and Summary

We have performed a simulation of the Ly $\alpha$  absorption spectrum originating from the low density IGM using a semi analytic ansatz. We have studied the effect of various parameters

Table 2: Comparison between simulated column density distribution and observations. The observed value of  $\beta_{\text{HI}}$  is around 1.35 at  $z = 2.31$  in the column density range  $12.8 \leq \log(N_{\text{HI}}/\text{cm}^{-2}) \leq 16.0$  (Kim et al 1997). The value of  $f$  and  $T_0$  are  $0.026^2$  and  $1.5 \times 10^4\text{K}$  respectively.

$\gamma$	$\beta_{\text{HI}}$
1.5	$1.24 \pm 0.12$
1.7	$1.31 \pm 0.13$
2.1	$1.44 \pm 0.14$

on the spectrum and the concerned statistics. We have found that our simulations match most of the observations available for a narrow parameter range.

(i) Various statistics performed on the simulated data and the observed points provided by McDonald (2000a) over a redshift range 2.09–2.67, constrain the value of  $f$  within  $0.020^2$ – $0.032^2$ , independent of  $T_0$  and  $\gamma$ . In this range of  $f$ , we considered three particular values of  $f$ , namely,  $0.023^2$ ,  $0.026^2$  and  $0.029^2$ . We constrain  $T_0$  within  $(0.8\text{--}2.5)\times 10^4\text{K}$  and  $\gamma$  within 1.3–2.3. If the range in  $f$  is narrowed down through some other studies, the values of  $\gamma$  and  $T_0$  can be constrained further. Although the observations allow  $f$  in the range  $0.020^2$  to  $0.032^2$ , we find that the match between simulations and observations is best for  $f \sim 0.026^2$ .

The values of  $T_0$  and  $\gamma$  are usually obtained (in previous attempts) from observational data through the Voigt profile fitting and the lower envelope  $N_{\text{HI}} - b$  scatter plot. The range obtained by us is consistent with the one obtained by Schaye et al. (2000). They infer  $1.26 \times 10^4\text{K} < T_0 < 2.00 \times 10^4\text{K}$  and  $\gamma = 1.45 - 1.65$  for the spectrum of QSO Q1442 at  $z = 2.5$  (see their Figure 6). McDonald et al. (2000b) use the lower cutoff of the  $N_{\text{HI}} - b$  scatter plot to infer  $T_0$  and  $\gamma$ . For  $\bar{z} = 2.4$ , they find  $T_0 = (1.74 \pm 0.19) \times 10^4\text{K}$ ,  $\gamma = 1.52 \pm 0.14$  or  $T_0 = (1.92 \pm 0.2) \times 10^4\text{K}$ ,  $\gamma = 1.51 \pm 0.14$ , depending on whether they calibrate the data using the output from hydrodynamical simulations at  $z = 3$  or  $z = 2$ , respectively. On the other hand, the hydrodynamical simulations (McDonald et al. 2000a) give slightly lower values of  $T_0$ , i.e.,  $T_0 = 1.31 \times 10^4\text{K}$  and  $1.6 \times 10^4\text{K}$ , for  $z = 2$  and  $z = 3$ , respectively. Ricotti et al. (2000) also use the  $N_{\text{HI}} - b$  scatter plot to constrain  $T_0$  between  $(1\text{--}2.4)\times 10^4\text{K}$  at  $z = 1.90$  and between  $(2\text{--}2.7)\times 10^4\text{K}$  at  $z = 2.75$ . The corresponding constraints on  $\gamma$  are  $1.32 \pm 0.30$  at  $z = 1.90$  and  $1.22 \pm 0.10$  at  $z = 2.75$ . For clarity, we show how our results compare with those obtained by other people in Figure 7. It should be clear from the figure and from the above discussion that our results are in quite good agreement with others.

It should, however, be stressed that the results obtained using the Voigt profile decomposition and  $N_{\text{HI}} - b$  scatter plot have certain inherent biases when compared with those obtained from the transmitted flux. For low column density clouds, the error is introduced in the  $b$  values because of the noise in the spectrum. Also considerable fraction of low col-

Table 3: The correlation function for Ly $\alpha$  clouds within  $100 \text{ km s}^{-1} < \Delta v < 150 \text{ km s}^{-1}$  for  $f = 0.026^2$ ,  $T_0 = 1.5 \times 10^4\text{K}$  and different values of  $\gamma$ , obtained from the simulations.

$\gamma$	$\xi_{\text{cloud}}(100 \text{ km s}^{-1} < \Delta v < 150 \text{ km s}^{-1})$
1.5	1.42
1.7	1.70
2.1	2.65

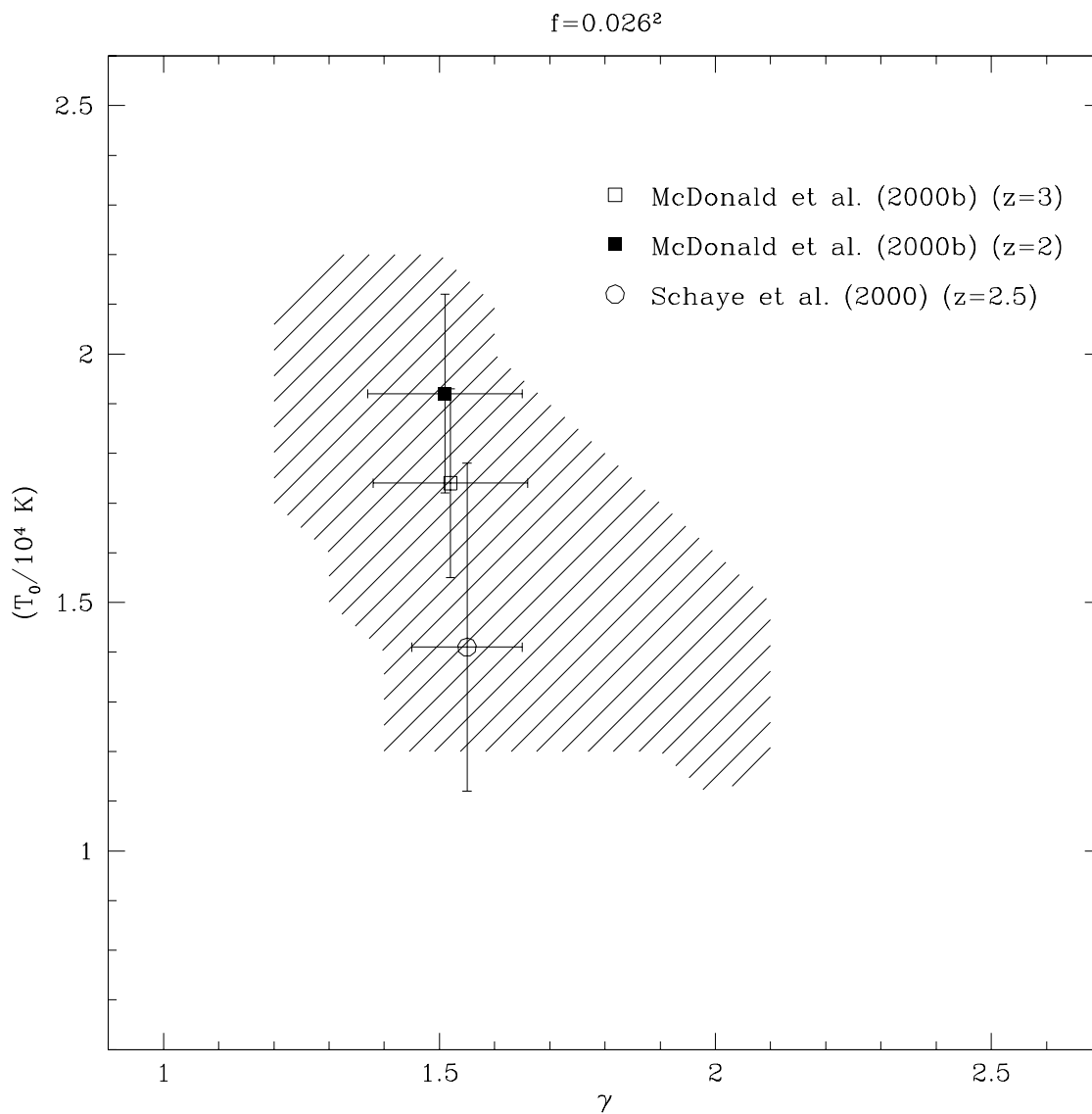


Fig. 7.— Comparison of the bounds on  $\gamma$  and  $T_0$  obtained by us with other results. The shaded region shows the bound from this work for  $f = 0.026^2$ . The open and the filled squares denote the parameter values obtained by McDonald et al. (2000b) depending on whether they use the output from hydrodynamical simulations at  $z = 3$  or  $z = 2$ , respectively. The value obtained by Schaye et al. (2000) for QSO Q1442 around  $z = 2.5$  is denoted by the open circle.



umn density low  $b$  lines that may not trace the low density regions are artificially introduced to get a better  $\chi^2$  while fitting the blends of saturated lines. For the high column density clouds, due to saturation, there is a degeneracy between velocity dispersion and number of components to be fitted. Our constraints on  $\gamma$  and  $T_0$  using the transmitted flux statistics are free from the above mentioned effects. These constraints on  $\gamma$  and  $T_0$  can be used simultaneously to constrain the reionisation epoch and the reionisation temperature (Hui & Gnedin 1997).

(ii) We constrain  $f = (\Omega_B h^2)^2 / J_{-12}$  to be in the range  $0.020^2 - 0.032^2$  regardless of the values of  $T_0$  and  $\gamma$ . The values for  $f$  found by McDonald et al. (2000a) are  $(0.0257 \pm 0.0017)^2$  (for  $T_0 = 1.31 \times 10^4 \text{K}$ ) and  $(0.0239 \pm 0.0016)^2$  (for  $T_0 = 1.6 \times 10^4 \text{K}$ ) for  $z = 2$  and  $z = 3$ , respectively. This is consistent with the range found in our study.

The constraint we have obtained on  $f$  is important because of the bound it implies on the baryon fraction of the universe. The situation is illustrated in Figure 8, where we plot  $\Omega_B h^2$  as a function of  $J_{-12}$ . The lower horizontal band corresponds to  $0.0170 < \Omega_B h^2 < 0.0208$ , which is considered to be the acceptable range of values from Big Bang Nucleosynthesis (BBN) (Burles, Nollett & Turner 2000). As has been noted by several authors and emphasised by Padmanabhan & Sethi (2000), this is already in contradiction with the 95 per cent confidence limits on  $\Omega_B h^2$  arising from the analysis of the initial BOOMERANG and MAXIMA data. The latter bound ( $0.025 < \Omega_B h^2 < 0.035$ ) is shown in the upper horizontal band in Figure 8 (for details see Bond et al. 2000; Padmanabhan & Sethi 2000). The bound on  $\Omega_B h^2$  arising from the current work ( $0.020 < \Omega_B h^2 / \sqrt{J_{-12}} < 0.032$ ) is shown as a function of  $J_{-12}$  by the curved band running from left bottom to the right top. It is clear from the figure that if  $J_{-12} > 1.2$  (indicated by the vertical dashed line in the figure), we have  $\Omega_B h^2 > 0.022$ , which is in violation of BBN value. Haardt & Madau (1996), using the QSO luminosity function, have estimated  $J_{-12} = 1.63$  for  $\Omega_m = 0.2$  open universe and  $J_{-12} = 1.13$  for  $\Omega_m = 1.0$  flat universe at  $z = 2.41$ . This can be considered as a strict lower bound on  $J_{-12}$ , as galaxies also contribute equally to the ionising UV background at these redshifts (Steidel, Pettini & Adelberger 2000). The bounds obtained from the proximity effect are  $0.9 < J_{-12} < 3.1$  (Scott et al. 2000). Thus, it appears that the bounds on  $\Omega_B h^2$  obtained from the Ly $\alpha$  forest analysis could possibly be inconsistent with those obtained from the BBN.

While this paper was being refereed, three groups have released further data (Netterfield et al. 2001, Pryke et al. 2001 and Stompor et al. 2001) with some initial analysis of their implications. The BOOMERANG group has given the best bet values of  $\Omega_B h^2 \approx 0.02$  which is consistent with BBN results (Netterfield et al. 2001). However, other group still obtains  $\Omega_B h^2 \approx 0.03$  (Stompor et al. 2001). There has also been a suggestion (Pettini & Bowen, 2001) that the a reanalysis of deuterium abundance might raise the BBN bound upwards to

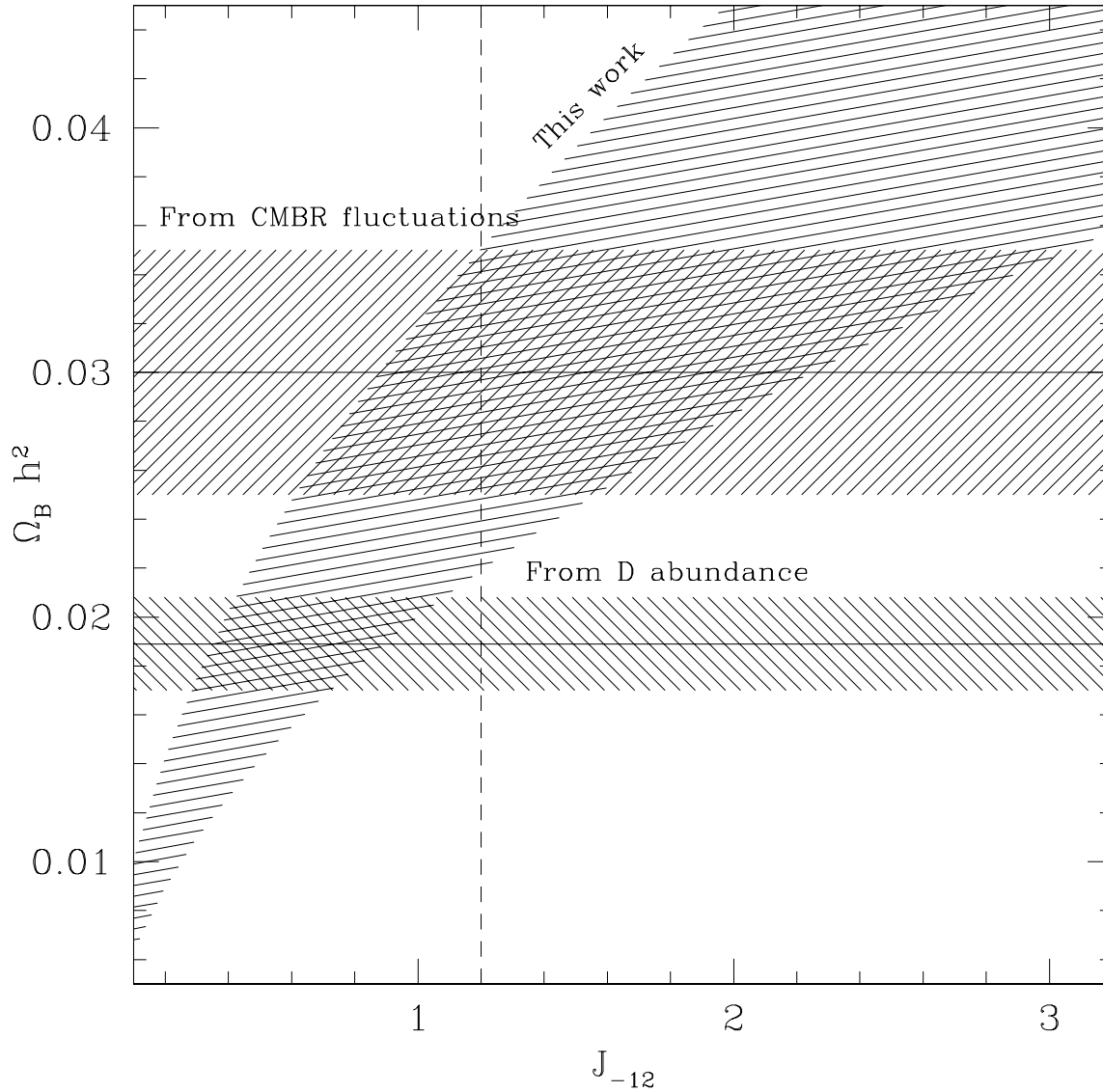


Fig. 8.— Comparison of the bounds on  $\Omega_B h^2$  obtained from our simulations with those obtained from Big Bang Nucleosynthesis (BBN) and CMBR analyses. The lower horizontal bound shows the region allowed by BBN (Burles, Nollett & Turner 2000) while the upper band shows that allowed by initial BOOMERANG and MAXIMA data (Bond et al. 2000; Padmanabhan & Sethi 2000). The bound on  $\Omega_B h^2$  arising from the current work is shown as a function of  $J_{-12}$  by the curved band running from left bottom to the right top.

about  $\Omega_B h^2 \approx 0.025$ . The situation is therefore unclear at present and these aspects must be kept in mind while assessing the importance of the results in Fig. 8. As far as the studies on IGM are concerned, we believe that it is important to estimate the value of  $J_{-12}$  more rigorously so as to put a strong constraint on  $\Omega_B h^2$ . Further work in this direction is in progress.

### Acknowledgment

We gratefully acknowledge the support from the Indo-French Centre for Promotion of Advanced Research under contract No. 1710-1. TRC acknowledges financial support from the University Grants Commission, India. We also thank McDonald et al. (2000) for making the observational data public.

### REFERENCES

- Bergeron J., Boisse P., 1991, A&A, 243, 344
- Bi H., 1993, ApJ, 405, 479
- Bi H., Davidsen A. F., 1997, ApJ, 479, 523 (BD)
- Bi H. G., Börner G., Chu Y., 1992, A&A, 266, 1
- Bi H., Ge J., Fang L., 1995, ApJ, 452, 90
- Black J. H., 1981, MNRAS, 197, 553
- Bond J. R., Szalay A. S., Silk J., 1988, ApJ, 324, 627
- Bond J. R., Ade P., Balbi A., Bock J., Borrill J., Boscaleri A., Coble K., Crill B., et al., 2000, preprint (astro-ph/0011378)
- Bryan G. L., Machacek M. E., 2000, ApJ, 534, 57
- Burles S., Nollett K. M., Turner M. S., 2000, preprint (astro-ph/0010171)
- Carlberg R. G., Couchman H. M. P., 1989, ApJ, 340, 47
- Cen R. Y., Miralda-Escudé J., Ostriker J. P., Rauch M. R., 1994, ApJ, 437, L9

- Choudhury T. R., Padmanabhan T., Srianand R., 2000, MNRAS, in press (preprint astro-ph/0005252) (Paper I)
- Coles P., Jones B., 1991, MNRAS, 248, 1
- Coles P., Melott A. L., Shandarin S. F., 1993, MNRAS, 260, 765
- Croft R. A. C., Weinberg D. H., Katz N., Hernquist L., 1998, ApJ, 495, 44
- Croft R. A. C., Weinberg D. H., Pettini M., Hernquist L., Katz N., 1999, ApJ, 520, 1
- Cristiani S., D’Odorico S., D’Odorico V., Fontana A., Giallongo E., Moscardini L., Savaglio S., 1997, in Petitjean P., Charlot S. ed., Proc. of the 13<sup>th</sup> IAP Astrophysics Colloquium, Structure and Evolution of the Intergalactic Medium from QSO Absorption Line Systems. Editions Frontières, Paris, p. 165
- Davé R., Hernquist L., Katz N., Weinberg D. H., 1999, ApJ, 511, 521
- Doroshkevich A. G., Shandarin S. F., 1977, MNRAS, 179, 95
- Efstathiou G., Bond J. R., White S. D. M., 1992, MNRAS, 258, 1P
- Eke V. R., Cole S., Frenk C. S., 1996, MNRAS, 282, 263
- Fang L. Z., Bi H., Xiang S., Börner G., 1993, ApJ, 413, 477
- Gnedin N. Y., 1998, MNRAS, 299, 392
- Gnedin N. Y., Hui L., 1996, ApJ, 472, L73
- Haardt F., Madau P., 1996, ApJ, 461, 20
- Hernquist L., Katz N., Weinberg D. H., Miralda-Escudé J., 1996, ApJ, 457, L51
- Hui L., 1999, ApJ, 516, 519
- Hui L., Gnedin Y. G., 1997, MNRAS, 292, 27
- Hui L., Gnedin Y. G., Zhang Y., 1997, ApJ, 486, 599
- Khare P., Srianand R., York D. G., Green R., Welty D., Huang K., Bechtold J., 1997, MNRAS, 285, 167
- Kim T., Hu E. M., Cowie L. L., Songaila A., 1997, AJ, 114, 1
- Kofman L., Gnedin N., Bahcall N., 1993, ApJ, 413, 1

- Kulkarni V. P., Huang K., Green R. F., Bechtold J., Welty D. E., York D. G., 1996, MNRAS, 279, 197
- Lomb N. R., 1976, Ap&SS, 39, 447
- McDonald P., Miralda-Escudé J., Rauch M., Sargent W. L. W., Barlow T. A., Cen R., Ostriker J. P., 2000a, ApJ, 543, 1
- McDonald P., Miralda-Escudé J., Rauch M., Sargent W. L. W., Barlow T. A., Cen R., 2000b, preprint (astro-ph/0005553)
- Mcgill C., 1990, MNRAS, 242, 544
- Miralda-Escudé J., Cen R., Ostriker J. P., Rauch M., 1996, ApJ, 471, 582
- Netterfield C. B., Ade P. A. R., Bock J. J., Bond J. R., et al., 2001, preprint (astro-ph/0104460)
- Nityananda R., Padmanabhan T., 1994, MNRAS, 271, 976
- Ostriker J. P., Steinhardt P. J., 1995, Nat, 377, 600
- Padmanabhan T., 1996, MNRAS, 278, L29
- Padmanabhan T., Sethi S. K., 2000, Ap. J (in press); (astro-ph/0010309)
- Pettini, M., Bowen, D. V. 2001, preprint (astro-ph/0104474)
- Press W. H., Teukolsky S. A., Vetterling W. T., Flannery B. P., 1992, Numerical recipes in FORTRAN. Cambridge: University Press
- Pryke C., Halverson N. W., Leitch E. M., Kovac J., Carlstrom J. E., 2001, preprint (astro-ph/0104490)
- Rauch M., Miralda-Escudé J., Sargent W. L. W., Barlow T. A., Weinberg D. H., Hernquist L., Katz N., Cen R., et al., 1997, ApJ, 489, 7
- Ricotti M., Gnedin N. Y., Shull J. M., 2000, ApJ, 534, 41
- Riediger R., Petitjean P., Mückel J. P., 1998, A&A, 329, 30
- Sargent W. L. W., Young P. J., Boksenberg A., Tytler D., 1980, ApJS, 42, 41
- Scargle J. D., 1982, ApJ, 263, 835

- Schaye J., Theuns T., Leonard A., Efstathiou G., 1999, MNRAS, 310, 57
- Schaye J., Theuns T., Rauch M., Efstathiou G., Sargent W. L. W., 2000, MNRAS, 318, 817
- Scott J., Bechtold J., Dobrzycki A., Kulkarni V. P., 2000, ApJS, 130, 67
- Srianand R., 1996, ApJ, 462, 68
- Srianand R., 1997, ApJ, 478, 511
- Srianand R., Khare P., 1994, MNRAS, 271, 81
- Srianand R., Khare P., 1996, MNRAS, 280, 767
- Steidel C. C., 1993, in Shull J. M., Thronson H. A., eds, Proc. of the 3rd Teton Astronomy Conference, The Environment and Evolution of Galaxies. Dordrecht, Kluwer, p. 263
- Steidel C. C., Pettini M., Adelberger K. L., 2000, preprint (astro-ph/0008283)
- Stompor R., Abroe M., Ade P., Balbi A., et al., 2001, preprint (astro-ph/0105062)
- Theuns T., Leonard A., Efstathiou G., 1998, MNRAS, 297, L49
- Theuns T., Leonard A., Efstathiou G., Pearce F. R., Thomas P. A., 1998, MNRAS, 301, 478
- Webb J. K., 1987, PhD thesis, Cambridge Univ.
- Zhang Y., Anninos P., Norman M. L., 1995, ApJ, 453, L57